Arabian Journal of Chemistry (2022) **15**, 103744

King Saud University

Arabian Journal of Chemistry

www.ksu.edu.sa
www.sciencedirect.com

ORIGINAL ARTICLE

Ferroelectric and photoelectrochemical studies of lead-free $Ba_{0.925}Bi_{0.05}\square_{0.025}(Ti_{0.65}Zr_{0.30}Sn_{0.05})O_3$ ceramic and its application to Rhodamine B oxidation under solar light

N. Haddadou [a], G. Rekhila [b,*], M. Benyoussef [c], K. Taïbi [a], A. Lahmar [c], M. Trari [b,*]

[a] *Crystallography-Thermodynamics Laboratory, Faculty of Chemistry, USTHB, P.O. Box 32, 16111 Algiers, Algeria*
[b] *Laboratory of Storage and Valorization of Renewable Energies, Faculty of Chemistry, U.S.T.H.B., BP 32, 16111 El-Alia, Algiers, Algeria*
[c] *Laboratory of Condensed Matter Physics (LPMC), University of Picardie Jules Verne, 33 Rue Saint-Leu, 80039 Amiens, France*

Received 21 October 2021; accepted 25 January 2022
Available online 10 February 2022

KEYWORDS

Lead-free perovskite;
Relaxor behavior;
Dielectric properties;
Photocatalysis;
Solar light

Abstract New materials with general formula $Ba_{0.925}Bi_{0.05}\square_{0.025}(Ti_{0.65}Zr_{0.30}Sn_{0.05})O_3$ (symbolized BBiTZS) were prepared by high-temperature solid-state reaction. The room X-ray diffraction pattern suggests a cubic perovskite structure. The thermal variation of the permittivity at different frequencies showed a relaxor ferroelectric behavior. The Raman spectroscopy was in accordance of the dielectric measurements. The diffuse phase transition parameters were determined from the modified Curie–Weiss law, while the relaxor behavior was highlighted by a good fit to the Vogel–Filcher relationship. The capacitance-potential ($C_{sc}^{-2} - E$) graph at pH ~ 7 is characteristic of *n*-type behavior with a flat band potential (E_{fb}) of −0.52 V_{SCE} and an electron density (N_A) of 2.7×10^{18} cm^{-3}. The Electrochemical Impedance Spectroscopy, measured in the region (1 mHz - 10^5 Hz), showed a semicircle, assigned with the bulk property (27 kΩ cm^2); a constant phase element (CPE) is responsible for the depletion angle (−9°). With an optical of 2.00 eV, the ferroelectric BBiTZS possesses appealing photocatalytic capability and was successfully experimented for the oxidation of Rhodamine B (Rh B) exposed to solar light. According to the band diagram, electrons from the conduction band of BBiTZS are injected into dissolved oxygen, resulting in $O_2^{\cdot}$ radicals, which are employed in the Rh B oxidation. UV–Visible spectrophotometry was used to follow the Rh B dis-

* Corresponding authors.
E-mail addresses: rekhilagharib@gmail.com (G. Rekhila), mtrari@usthb.dz (M. Trari).
Peer review under responsibility of King Saud University.

Production and hosting by Elsevier

https://doi.org/10.1016/j.arabjc.2022.103744

coloration. On a solar irradiation of 97 mW cm^{-2}, a conversion of 50% is achieved in Rh B solution (10 mg L^{-1}) within 100 min., and the degradation follows a first order kinetic model with a half photocatalytic-life of 90 min.

1. Introduction

Ferroelectric materials of perovskite structure (ABO_3) have been intensively investigated due mainly to their high-performance properties. These materials are of paramount utility in various applications; one can cite the capacitors, actuators, transducers etc … (Kenji uchino, 1994; Park et al., 1999; Alexe et al., 1999). Nevertheless, the majority of them are lead-based ceramics, which has resulted in environmental problems due to the volatility of the hazardous lead oxide. The toxicity of various species has led to the adoption of a universal law restricting the utilization of harmful compounds (metals, pesticides, dyes etc…) (Directive 2011/65/EU, 2011). This is the case of lead-based compounds whose use is currently prohibited. Therefore, contemporary research is now focused on the discovery of new environmentally friendly materials that could be as efficient as the lead compounds used in the manufacture of electronic devices. In this view, specific interest has been devoted to the ferroelectric materials with highly polarized network. This is the case of ferroelectric compounds containing the lone pair cation Bi^{3+} ions, which are distinguished by the presence of lone paire electron. Indeed, in these ferroelectric materials, the internal dipole field can cause a separation of the electron/hole (e^-/h^+) pairs the reduction and the reduction / oxidation reactions, thus improving the separation of the charge carriers. In fact, the intrinsic spontaneous polarization induces macroscopic charges on the material surface, which are composed by free carriers and defects in the bulk ferroelectric (internal screening) and/or by charged molecules adsorbed by the environment (external screening) (Yang et al., 2005). Such behavior is desirable for photo-electrochemical applications (Burbure et al., 2010a,b; Giocondi and Rohrer, 2001). In addition, the recent literature indicates that the combined ferroelectric / photoelectrochemical properties could strongly improve the photocatalytic performance (Lin et al., 2007). Besides, the separation of charge carriers is due to the influence of the ferroelectric nature on the bending of the bands, which helps to inhibit the recombination of (e^-/h^+) pairs, almost similar to the *p-n* junction of a typical photovoltaic or diode structure. Indeed, ferroelectric materials mask the surface depolarization field by developing strong Stern layers with chemisorbed molecules (Cui et al., 2013).

$BaTiO_3$ (BT) has deserved a particular attention in this field and a tetragonal / cubic transition occurs at a critical particle size of 0.12 μm at room temperature (RT), and the Curie temperature (T_C) drops below room temperature at the critical particle size. Therefore, both the non-ferroelectric-cubic and the tetragonal-ferroelectric phases coexist at RT. Thus, BT acts only as a traditional wide band gap semiconductor under UV light excitation (Uchino et al., 1989). Several works have been conducted in order to improve the photocatalytic properties of BT, where the tetragonal phase has better catalytic activity than cubic one (Kappadan, 2016). Further, the photocatalytic performance is improved through the development of a nanostructured metallic coating of Ag on its surface. Alternatively, BT-based ferroelectric relaxers endorse interesting photoelectrochemical characteristics combined with ferroelectric ones (Boutal et al., 2014; Kerfah et al., 2011; Bensemma et al., 2018; Haddadou et al., 2018a) and Qi et al. reported 15% degradation of Rhodamine B (Rh B) solution onto the relaxer $BaBi_4Ti_4O_5$ under UV–Vis irradiation (Qi et al., 2019). Owing to its electropositive character, Bismuth in the relaxor $Ba_{0.785}Bi_{0.127}Y_{0.017}TiO_3$ leads to a weaker covalency of Ti–O bond and therefore a destabilization of the conduction band (CB) ($\pi^*_{Ti\text{-}O}$) (Kerfah et al., 2011). It is interesting to mention that the BT based materials showed a photocatalytic efficacy upon ultraviolet light (Tang et al., 2004; Reddy et al., 2016) and the statistical fluctuations of ions in A and/or B sites improve the ferroelectric and photoelectric properties. In this work, we emphasis the investigations of photoelectrochemical properties of lead-free ferroelectric composition $Ba_{0.925}Bi_{0.05}\square_{0.025}(Ti_{0.65}Zr_{0.30}Sn_{0.05})O_3$ (abbreviated BBiTZS).

The present composition is distinguished by the dual substitution in the A-site (Ba-Bi) and B-site (Ti-Zr-Sn) which improves the relaxor effect and stimulates the phase transition diffuse character. In addition, the presence of Bi^{3+} with 6 s^2 lone pair contributes favorably to the photocatalytic activity (Wang and Wang, 2012; Ai et al., 2014). In addition, the ferroelectric materials with a relaxor behavior has an extended depletion width, an attractive property for the photo-electrochemical applications (Li et al., 2009; Yang et al., 2006). In this paper, we present a selected relaxor ferroelectric composition (x = 0.05 and y = 0.30) to appreciate its photoelectrochemical behavior. This composition belongs respectively to the solubility domain of Bi in BBiTZS and to the relaxor ferroelectric domain.

The Rhodamine B (Rh B), employed as tracer in water, was selected to evaluate the photoactivity of BBiTZS. It is also used as a staining fluorescent dye tunable at 610 nm. It is suspected to be carcinogenic and its elimination is of high priority. In this regard, the advanced oxidation processes (AOPs) are well known for the dyes degradation under soft conditions, yielding to a high mineralization. In this regard, wide band gap ferroelectrics were successfully used for the generation of (e^-/h^+) pairs, involved in the reactive radicals $O_2^{\cdot}$ and/or $OH^{\cdot}$ respectively in the conduction band (CB) and valence band (VB) with a high oxidative power.

2. Experimental procedure

2.1. Materials preparation

Pure powders of $BaCO_3$, Bi_2O_3, TiO_2, ZrO_2, and SnO_2 (all Sigma Aldrich) were used as starting materials; they were previously dried at 200 °C (3 h) to eliminate the adsorbed water. The ceramic of composition $Ba_{0.925}Bi_{0.05}\square_{0.025}(Ti_{0.65}Zr_{0.30}Sn_{0.05})O_3$ have been prepared by solid-state reaction, as described below:

$$0.925\ BaCO_3 + 0.025\ Bi_2O_3 + 0.65\ TiO_2 + 0.30\ ZrO_2 + 0.05 SnO_2 \rightarrow$$

$$Ba_{0.925}Bi_{0.05}\square_{0.025}(Ti_{0.65}Zr_{0.30}Sn_{0.05})O_3 + 0.925\ CO_2 \quad (1)$$

where "□" is the vacancy formed during the high temperature reaction. Thereafter, the powders were weighed in the stoichiometric amounts and ground in an agate mortar for 2 h. Then, the mixture was heat-treated under air atmosphere at 850 °C (15 h) with a heating rate of 5 °C/min. Finally, the resulting powder was pressed under 500 MPa into pellets (13 mm diameter and ~ 1 mm thickness) and sintered at 1200 °C (4 h) under air atmosphere. Loss of weight was determined before and after heat treatment and was found to be less than 1%. Diameter shrinkages $\Delta\Phi/\Phi$ were determined as ($\Phi_{initial} - \Phi_{fi}$-

$_{nal})/\Phi_{initial}$. Their values were about 10% while the relative density (experimental density/theoretical density) was about 0.90.

2.2. Characterization

However, the identification of the phase, the related symmetry and the unit-cell parameters were achieved using a D8 Advance X-ray diffractometer (Vantack detector). The data were collected at room temperature using $Cu_{K\alpha 1+2}$ radiation in the 2θ range (10–80°). Scanning electron microscopy (SEM) of the ceramic was obtained with a Philips XL30 microscope. The Raman spectrum was plotted with an Yvon Jobin T64000 spectrometer using Ar excitation laser line (514.5 nm).

The thermal dependence of the dielectric properties was performed in the temperature (100–450 K) and frequencies (10^2–0^6 Hz) ranges thanks to a Solartron Impedance Analyzer SI 1200.

The photo electrochemistry was studied in a conventional cell with Pt as auxiliary electrode and SCE as reference in neutral medium (Na_2SO_4, 0.1 M); the intensity-potential J(E) were plotted at a scan rate of 10 mV $s^{-}1$ while the capacitance was measured against the potential at a constant frequency of 10 kHz. The photocatalytic experiments were carried out in a batch mode in an open Pyrex reactor, exposed to direct sunlight. The solubility of Rh B in water is relatively high (~15 g/L). The powder catalyst (50 mg) was suspended in 100 mL of Rh B solution at a concentration of 50 mg/L at pH 7, with a dark adsorption duration of 30 min. The powder was centrifuged (3000 rpm, 15 min.) after each test to separate the powder from the electrolyte for the chemical analysis. The greatest sensitivity detection limit improves both the selectivity and resolution between the investigated compounds and degradation products. UV–Visible spectrophotometry (λ_{max} = 554-nm) was used to measure the remaining Rh B concentration (C_t).

3. Results and discussion

3.1. Microstructural study

Fig. 1 (a Inset) shows the microstructure of BBiTZS. The grains appear in square shape arranged with each other leading to few vacant spaces, giving rise to a high microstructural density. The histogram of grain distribution reveals small sizes

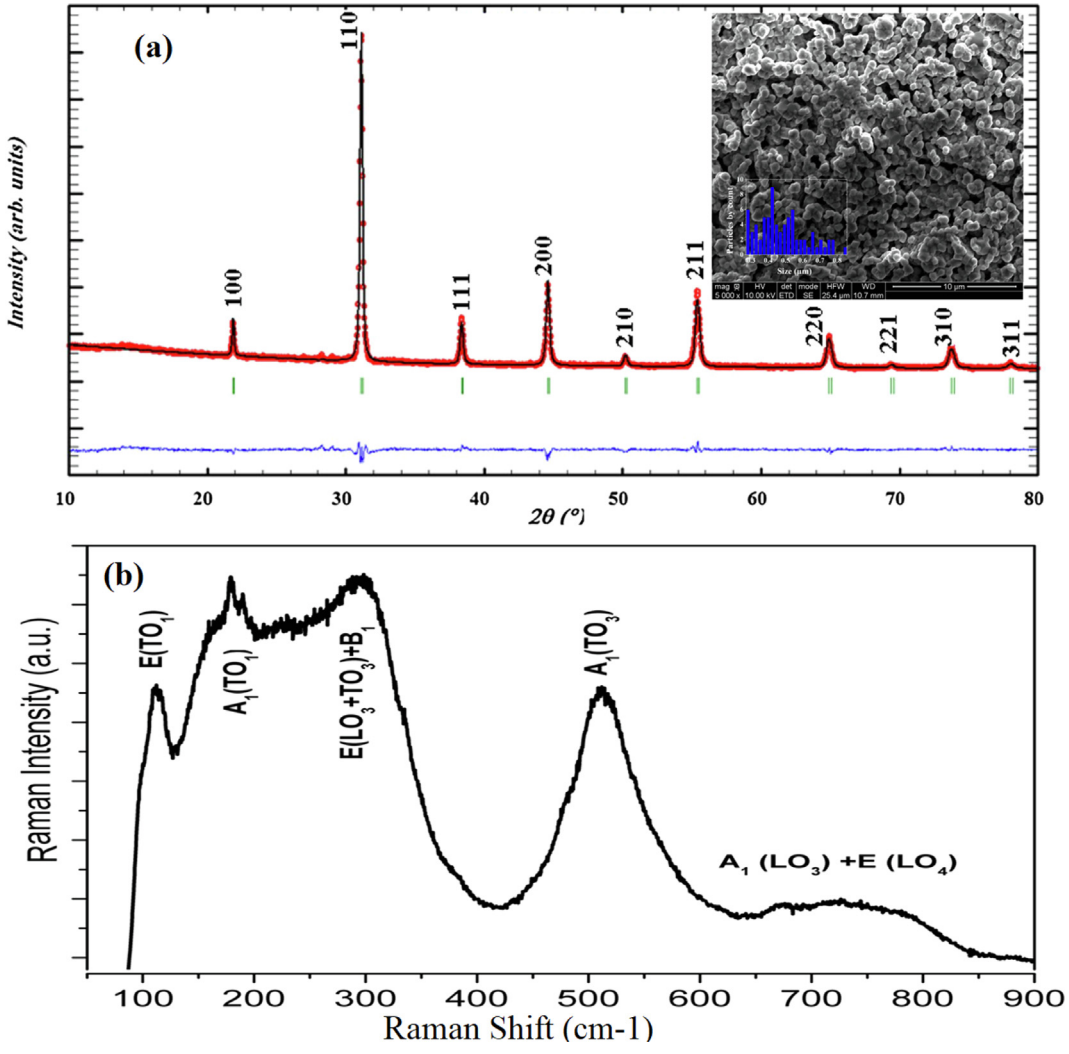

Fig. 1 Rietveld refinement and microstructure (Inset a) and Raman spectrum (b) for BBiTZS room temperature.

within this ceramic (0.3–0.8 μm). Tang et al. (2004) reported the grain size influence on the Ba $(Ti_{1-y}Zr_y)O_3$ system. They showed that the coarse-grained sample undergoes a structural phase transition, instead to a relaxor-like behavior for the fine-grained sample. As BBiTZS is distinguished by small grain sizes, we expected that it would behave as a relaxor ferroelectric as confirmed by the dielectric measurements (see below).

3.2. Room-temperature X-ray diffraction

The single phase formation of the BBiTZS sample was confirmed by XRD analysis at room temperature. The Rietveld refinement and calculation reliability factors were determined in the cubic symmetry ($Pm\bar{3}m$, JCPDS N°75-0461) using the Fullprof software (Boultif and Loueer, 1991) integrated in the Win PLOTR program (Rodríguez-Carvajal, 2002) where all the reflection peaks are indexed. A perfect agreement is observed between the observed XRD patterns and fitted data (Table 1). Moreover, the agreement between the observed and calculated inter-planer spacing suggests a cubic symmetry at room temperature.

Table 2 gathers the lattice parameters and refinement reliability factors obtained by the Rietveld refinement in comparison with those of BT. The fitting parameters (R_B, R_F, Rwp and χ^2) indicate good agreement between refined and observed XRD and confirm the cubic symmetry.

Table 3 assembles the refined atomic positions, occupancy and isotropic atomic shift parameters of BBiZTS composition. As it can be seen, Ba^{2+} and Bi^{3+} are located in the same A-site with a fractional percentage. In addition, $Ti^{4+}/Zr^{4+}/Sn^{4+}$ cations located in the B-sites are connected with the oxygen atoms to form $(Ti^{4+}/Zr^{4+}/Sn^{4+})O_6$ octahedra sharing corners. In addition, relatively good reliability factors (compared to standard values) are in the range of disordered perovskites with a tolerance factor below unity (Cross, 1994).

3.3. Raman analysis

The Raman spectrum of BBiTZS (Fig. 1b) confirms the observed active modes in the cubic symmetry, in agreement with the relaxor ferroelectric compositions. The assignment of the Raman modes is carried out by analogy with the $Ba_{1-x}Bi_xTi_{1-x}Yb_{x/2}Fe_{x/2}O_3$ and $BaZr_xTi_{1-x}O_3$ (Schileo et al., 2013; Dobal et al., 2001). The spectrum consists of six distinguished modes 110, 186, 256, 301, 518 and 720 cm^{-1} according respectively to the following modes: $E(TO_1)$, $A_1(TO_1)$, $A_1(TO_2)$, $E(TO_2)$, $A_1(TO_3)$ and $A_1(LO_3)$ + E(LO). The A_1TO_2 mode tends to disappear while the modes $A_1(LO_3)$ + E(LO) become wider. These observations are related to the fact that BBiZTS is in its paraelectric (cubic) phase at RT. We recall that the cubic -paraelectric phase allows 12 optical modes (3F1u + F2u) that are not Raman active However, for BBiTZS, the activation modes are caused by a considerable

Table 1 Powder diffraction data of $Ba_{0.925}Bi_{0.05}(Ti_{0.65}Zr_{0.30})Sn_{0.05}O_3$.

$2\theta_{obs}$[°]	$2\theta_{cal}$[°]	hkl	d_{cal}[Å]	I_{obs}/I_0[%]	I_{cal}/I_0[%]
21.853	21.868	100	4.0609	6	9
31.110	31.12	110	2.8715	100	100
38.359	38.36	111	2.3446	16	15
44.587	44.59	200	2.0305	33	35
50.185	50.19	210	1.8161	5	5
55.375	55.37	211	1.6579	36	34
64.896	64.89	220	1.4358	17	18
69.370	69.37	221	1.3536	2	2
73.719	73.71	310	1.2842	15	14
77.980	77.97	311	1.2244	3	4

Table 2 Symmetry, lattice parameters and refinement reliability factors of BBiZTS composition.

Compounds	a = b = c (Å)	V(Å^3)	Space group	R_B	R_F	Rp	R_{wp}	χ^2
BBiZTS	4.0627 (1)	67.06	$Pm\bar{3}m$	0.0540	0.756	9.19	7.81	1.37
$BaTiO_3$ (T)	3.9945	64.36	$Pm\bar{3}m$	–	–	–	–	

Table 3 Refined structural parameters of the BBiTZS cubic phase.

Atom	Site	x	y	Z	B(Å)	Occupancy
Ba/Bi	1a	0	0	0	0.69 (4)	0.8921/0.0478
Ti/Zr/Sn	1b	ø	ø	ø	0.75 (4)	0.6505/0.300/0.05
O	3c	ø	ø	0	0.98 (6)	3.064

structural disorder characterizing the ferroelectric relaxor (Dobal et al., 2001). The RT Raman study about the influence on the structural transition has been reported in detail in our previous work (Haddadou et al., 2018b; Smail, 2020).

3.4. Dielectric studies

3.4.1. Thermal variation of dielectric permittivity

The thermal variation relative permittivity (ε'_r) and dielectric losses (tg δ) of BBiTZS at various frequencies exhibit a single broad peak with a frequency dispersion compatible with a relaxor ferroelectric behavior (Fig. 2). Indeed, ε'_r increases gradually to a maximum value ε'_{rmax} with increasing temperature and then decreases smoothly indicating a phase transition. ε'_{rmax} and the corresponding temperature maximum (T_m) depend upon the measurement frequency. Indeed, BBiTZS exhibits a broad peak with a maximum ε'_{rmax} that decreases with increasing frequency. In addition, the temperature related to this maximum (T_m) shifts toward higher values as the frequency increases. All these dielectric characteristics agree with the ferroelectric relaxor behavior. Generally, the broadening of the dielectric peaks is attributed to some structural disorder generated by the compositional fluctuation in the crystalline network as can be considered for the present sample.

3.4.2. Ba^{2+}/Bi^{3+} substitution effect on the dielectric properties

BBiTZS may show a variety of defects imputed to different mechanisms. For instance, it could be related to apparent oxygen vacancies due to Bi_2O_3 volatility. Indeed, the order–disorder behavior in the complex perovskites $(AA')(BB')O_3$ has been largely studied. The statistical fluctuations of ions in the A and/or B sites produce a local heterogeneity leading to ferroelectric compounds with a large variation of the temperature T_C (Schileo et al., 2013). Concerning BBiZTS, Bi^{3+} behaves as donor level. Thence, charge disproportionality may arise while replacing Ba^{2+} by Bi^{3+} according the following equation (in Kroger-Vink notation):

$$BaO + Bi_2O_3 \rightarrow Ba_{Ba} + 2\,Bi_{Ba} + V''_{Ba} + 4\,O_o \qquad (2)$$

where V''_{Ba} is a cationic vacancy generated by the electrical neutrality condition. According to Eq. (2), two Bi^{3+} substituting Ba^{2+} ion and one A-site vacancy is formed by a charge mechanism compensation, leading to a local compositional fluctuation. The same behavior has been reported on the BZT system where the vacancies alter both the order–disorder and local symmetry of the material as well as the physical properties (Nag Bhargavi et al., 2018; Wang et al., 2020; Wang et al., 2021). These studies confirm that the introduction of Bi^{3+} into the Ba-site could effectively improve the energy storage performance in the relaxors ferroelectrics.

3.4.3. Deviation from Curie-Weiss law in BBiTZS

The dielectric constant of a normal ferroelectric obeys the Curie Weiss (C-W) law in the paraelectric phase. The following relation expresses this:

$$\frac{1}{\varepsilon'_r} = \frac{(T - T_o)}{C} (T > T_c) \qquad (3)$$

where C is the Curie constant and T_o the C-W temperature. The curve $1/\varepsilon'_r = f(T)$ (Fig. 3) allowed the determination of the corresponding constant C and T_o for BBiTZS. These values as well as the parameter ΔT_m (eq. (4)) are reported in Table 4:

$$\Delta T_m = T_{dev} - T_m \qquad (4)$$

T_{dev} is the temperature at which the dielectric permittivity begins to deviate from the C-W equation and T_m is the temper-

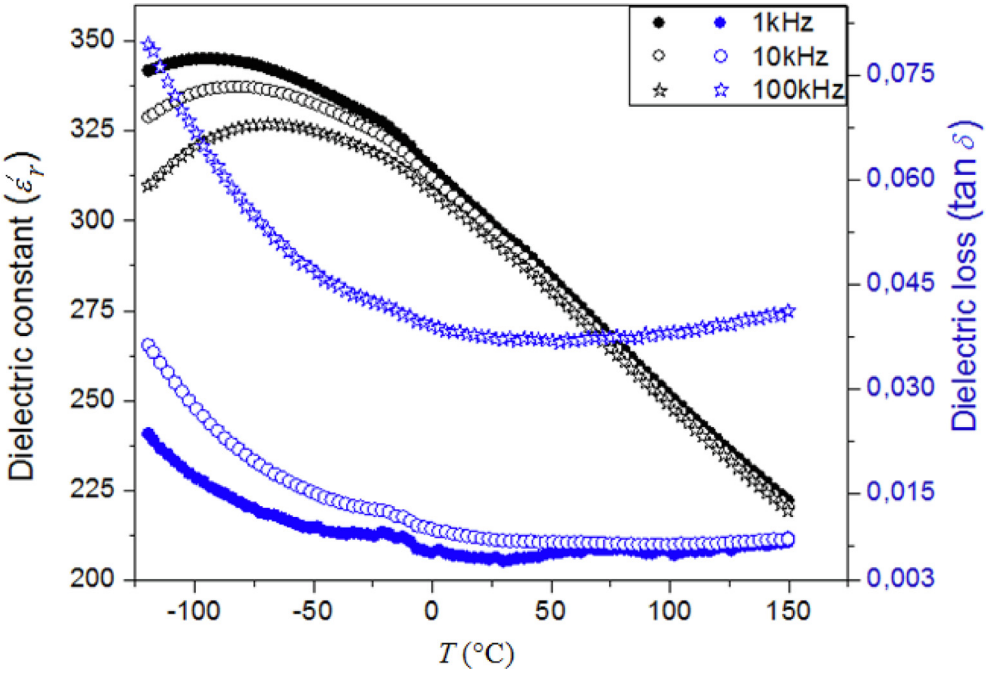

Fig. 2 Thermal evolution of the dielectric constant and dielectric losses at various frequencies for BBiTZS.

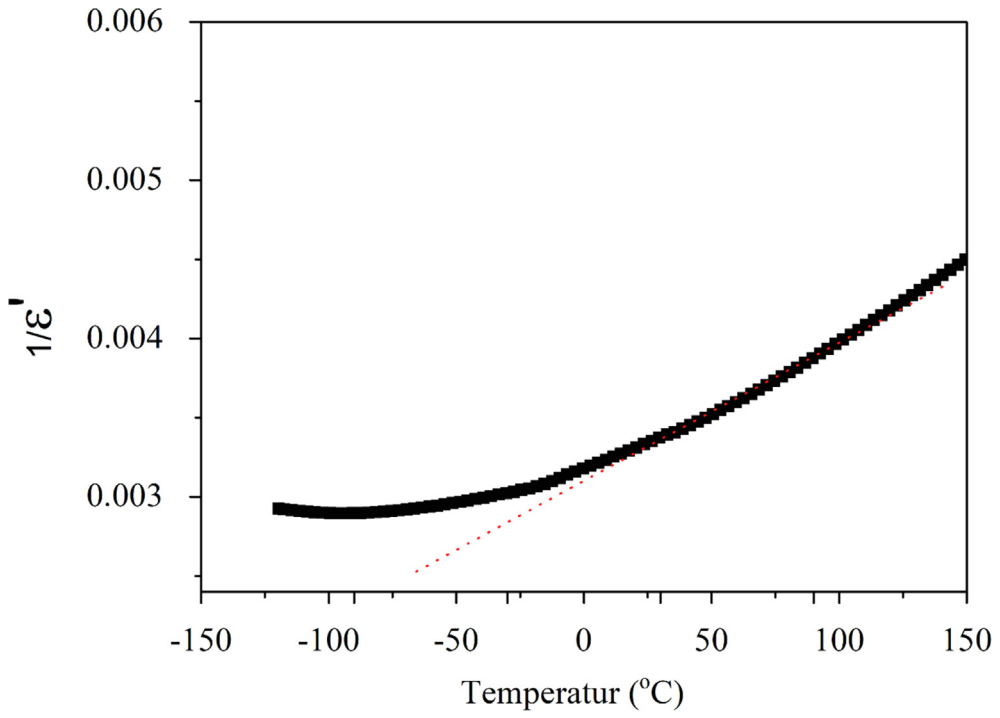

Fig. 3 Thermal variation of the inverse of the real part of the relative permittivity (ε'^{-1}) at 1 kHz for BBiTZS ceramic.

Table 4 Dielectric characteristics of the BBiTZS composition at 1 kHz.

parameters	T_m (°C)	T_0(°C)	T_{dev} (°C)	$C.10^{-5}$(°C)	ΔT_m (°C)	ΔT_{mf} (°C)	$\Delta\varepsilon'_r/\varepsilon'_r$	ε'_{rmax}	tg (δ)	γ
BBiTZS	−88	−261	83	1.09	171	16	0.045	345	0.016	1.80

ature corresponding toat which the maximum permittivity (Tang et al., 2005).

It should be noted the low values of T_m and ε'_{rmax} are certainly related to the dual association of Zr^{4+} and Sn^{4+} in the B site of BBiTZS. Indeed, it is well-known that the addition of Zr to $BaTiO_3$ leads to a relaxor effect and the temperature T_m decrease as the content of Zr increases (Ciomaga et al., 2007). The same behavior occurs when Sn substitutes Ti in $BaTiO_3$ (Jiwei et al., 2005; Xiaoyong et al., 2003). As the amount of Sn increases, the temperature of the ferroelectric-paraelectric transition decreases and the phase transition becomes more diffuse over a broad temperature range. Consequently, the combination of Zr and Sn to replace partially Ti leads to a synergistic phenomenon causing a large decrease in T_m. We observe for BBiTZS where the high quantity of Zr (0.30) gives rise to a very low temperature ($T_m = -88$ °C), far from room temperature.

3.4.4. Diffuse phase transition parameters of BBiTZS

Likewise, in order to quantify the diffuse phase transition nature within BBiTZS, we determined the diffusivity coefficient (γ) from the following relation (Uchino and Nomura, 1982):

$$\frac{1}{\varepsilon'_r}-\frac{1}{\varepsilon'_{rmax}}=\frac{(T-T_m)^{\gamma}}{C}\,(T>T_m) \tag{5}$$

with $1 \le \gamma \le 2$; $\gamma = 1$ and 2 are the limit values corresponding respectively to a normal ferroelectric behavior and to a completely disordered (i.e. relaxor system). This expression corresponds to the modified C-W law that allows the description of the diffuse character in the paraelectric phase. The curves of ln $(1/\varepsilon_r - 1/\varepsilon_{rmax})$ versus ln $(T - T_{max})$ at 1 kHz is shown in Fig. 4. A linear variation is obtained for this composition where the coefficient γ was computed by fitting the line; a γ value of 1.80 (Table 4) corroborates the diffuse nature of the phase transition for this composition.

3.4.5. Relaxor characteristics of BBiTZS

The relaxor ferroelectric behavior is marked by the frequency dependence of T_m and ε'_r. This typical comportment is evaluated from ΔT_{mf} and $\Delta\varepsilon'_r/\varepsilon'_r$:

$$\Delta T_{mf} = T_{mf(10^6\,Hz)} - T_{mf(10^2\,Hz)} \tag{6}$$

$$\Delta\varepsilon'_r/\varepsilon'_r = \varepsilon'_{r(10^2\,Hz)} - \varepsilon'_{r(10^6\,Hz)}/\varepsilon'_{r(10^2\,Hz)} \tag{7}$$

The frequency dispersion is more significant as ΔT_{mf} and $\Delta\varepsilon'_r/\varepsilon'_r$ are higher. $\Delta\varepsilon'_r/\varepsilon'_r$ (=0.045) indicates a weak relaxor behavior for the BBiTZS while the absence of frequency dispersion corresponds to $\Delta\varepsilon'_r/\varepsilon'_r = 0$.

3.4.6. The Vogel-Fülcher (V-F) analysis

The strong frequency dependence of T_m is supported by the curve ln f vs. T_m (Fig. 5). The nonlinear behavior indicates that the data cannot be adjusted with the Debye equation. To

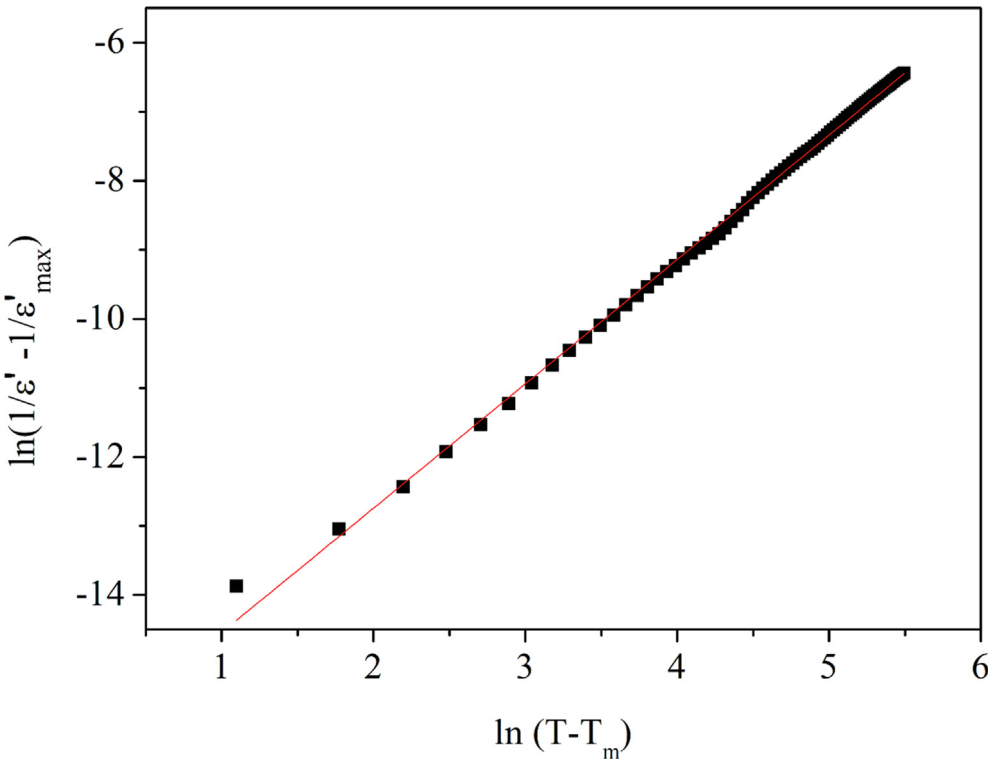

Fig. 4 Curves $\ln(1/\varepsilon_r - 1/\varepsilon_{max})$ versus $\ln(T\text{-}T_{max})$ at 1 kHz for BBiTZS composition.

analyze the principal relaxation features of this composition, the curve was fitted by the Vogel–Fülcher (V-F) equation (Viehland et al., 1991)

$$f = f_0 \exp \frac{E_a}{k_B(T_m - T_g)} \quad (8)$$

where f_o is the attempt frequency, E_a the average activation energy and T_g are the freezing temperature.

The V-F equation models the shift of T_m toward low values of frequencies. The close agreement of the data for BBiTZS with the V-F relationship suggests a relaxor behavior. The modeling parameters by the V-F relation confirm this assertion and attribute this effect to the presence of polar nano regions in the crystal lattice. These adjusted parameters are: E_a = 0.112 eV, T_g = 195 K and $f_o = 1.26 \times 10^7$ Hz.

It is helpful to outline that the compounds BBiTZS have a similar behavior to that of $Ba(Ti_{1-y}Zr_y)O_3$ solid solutions ($0.26 \leq y \leq 0.40$) (Laulhé, 2007). For these latter, it has been evidenced that the ZrO_6 and TiO_6 octahedra were deformed with a particular impact on the direction of local dipole moments carried by Ti^{4+} cations. A random distribution of the cations leads to a local polarization that would be at the origin of the frequency dispersion observed experimentally. All the ferroelectric features mentioned above are promising for photocatalytic applications.

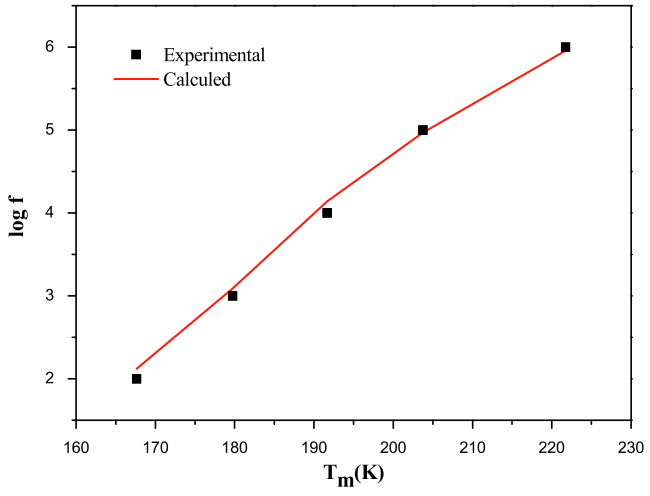

Fig. 5 Plot of ln(f) as a function of Tm for BBiTZS composition (the symbols: experimental data; the solid curve: fitting to the Vogel– Fulcher relation).

3.5. Impedance spectroscopy

The impedance spectroscopy is performed to study the relationship between the microstructure and electrical properties in the temperature range (RT – 100 °C). Fig. 6 presents the frequency dependent real and imaginary part of the impedance at various temperature (22–80 °C) for $Ba_{0.925}Bi_{0.05}(Ti_{0.65}Zr_{0.30}Sn_{0.05})O_3$. From the figure, we can observe the occurrence of the relaxation frequency for BBiTZS between 10^4 and 10^5 Hz. In the view to extract information on the resistive properties of the ceramic, we plotted the Cole-Cole plot of the impedance formalism at different temperatures (Fig. 6). We can observe from the plot, well-resolved semi-circles for the studied temperatures. Besides, the radius of the semi-circles decreases as the temperature increases, which demonstrates the semiconducting nature of our sample (Wang et al., 2017). By the use of

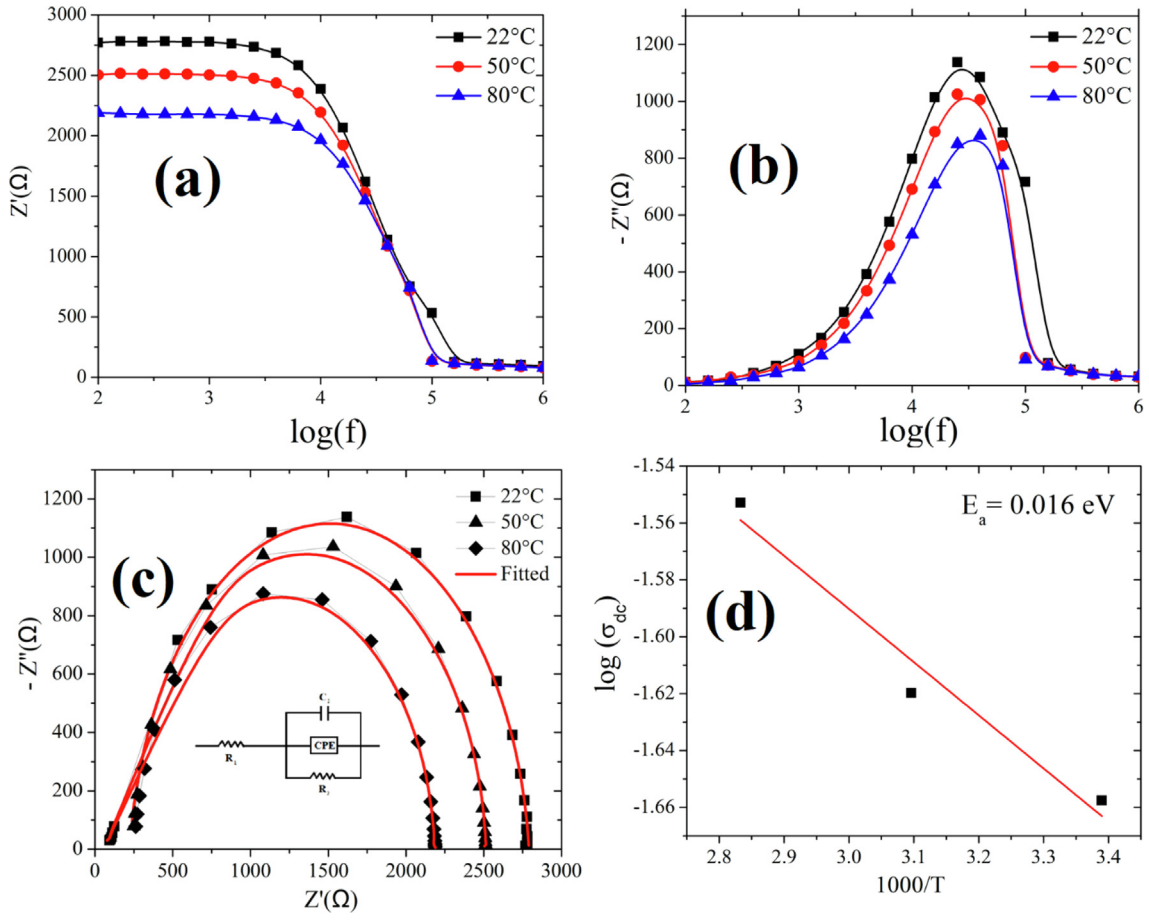

Fig. 6 (a) Real impedance Z′(f) curves, (b) Imaginary impedance Z″(f) curves of BBiTZS system at different temperatures, (c) Fitted Cole-Cole plots at different temperatures. The inset presents the model used to fit the BBiTZS system, (d) The Arrhenius plots of BBiTZS system. The activation energy extracted from the dc conductivity (at 10 kHz).

a model (Fig. 6c), we could fit the collected data. Our proposed model includes a serie resistance (R_1), in addition to the bulk contribution (R_2, C_2). Besides, a departure from the ideal Debye behaviour was observed and better fitting results were obtained by introducing constant phase element (CPE) in the circuit (Benyoussef et al., 2020) and Table 5 regroups the electrical parameters. We can observe that the bulk resistance decreases as the temperature increases, which demonstrates the Negative Temperature Coefficient of Resistivity of our studied ceramic. Fig. 6d shows the logarithmic scale of the dc conductivity versus 1000/T for our sample. The plot is observed to be linear and follows an Arrhenius equation $\left(\sigma = \sigma_0 \exp\left(-\frac{E_\alpha}{K_B T}\right)\right)$ (Lanfredi et al., 2000). The activation energy of the system was found to be 0.016 eV.

3.6. Electrochemical and photocatalytic properties

The optical characterization of BBiTZS is elucidated from the diffuse reflectance. The photon energy ($h\nu$,) absorption coefficient (α) and gap (E_g) are related by the equation (Rekhila et al., 2018):

$$(\alpha h\nu)^{1/m} = A\ (h\nu - E_g) \quad (9)$$

Table 5 Resistance and Capacitance parameters obtained from the fit.

T (°C)	R_1 (ohm)	R_2 (ohm)	C_2 (F)
22	223	2566	$1.17\ 10^{-9}$
50	240	2272	$1.12\ 10^{-10}$
80	252	1936	$1.03\ 10^{-10}$

The exponent $m = 2$ and 0.5 are respectively for indirect and direct transitions. The intersection of the line $(\alpha h\nu)^{0.5}$ with the abscissa axis yields the E_g value of the perovskite (2.00 eV) (Fig. 7). The defect states and grains boundaries have no influence on the thermo-power (S) unlike the conductivity (SM 1); the negative value implies that the free carriers are electrons. The non-dependence of S with temperature indicates thermal activation of the electronic concentration with a constant mobility ($=360\ \mu V\ K^{-1}$), the S-value is compatible with an order of magnitude of the electrons density (N_D) of $\sim 10^{19}$ cm^3 (see below).

The electrochemistry is of high importance for predicting the electrochemical reactions; the profile of the intensity-potential J(E) profile of BBiTZS (Fig. 8) shows a little hysteresis with a decomposition voltage greater than 3 V, char-

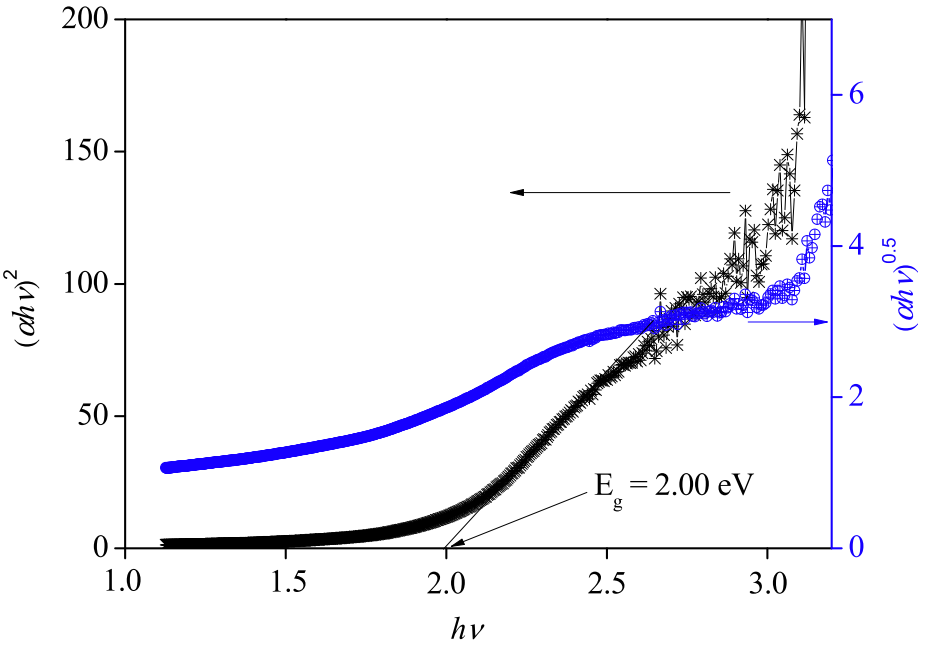

Fig. 7 The indirect $(\alpha h\nu)^{0.5}$ and direct $(\alpha h\nu)^2$ optical transitions of BBiTZS.

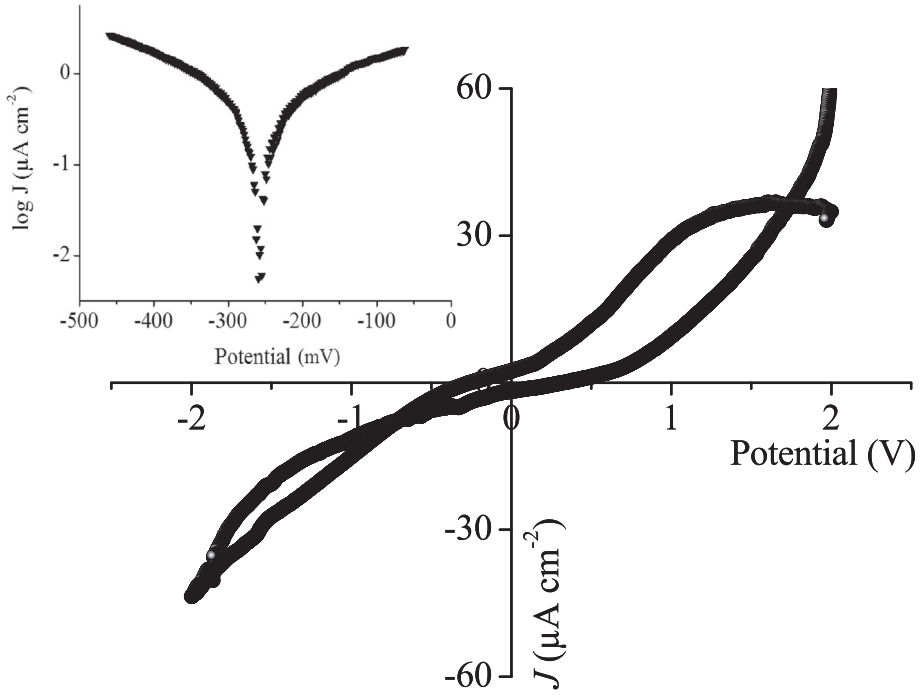

Fig. 8 The intensity–potential characteristic of BBiTZS in Na_2SO_4 electrolyte. **Inset**: the semi-logarithmic plot.

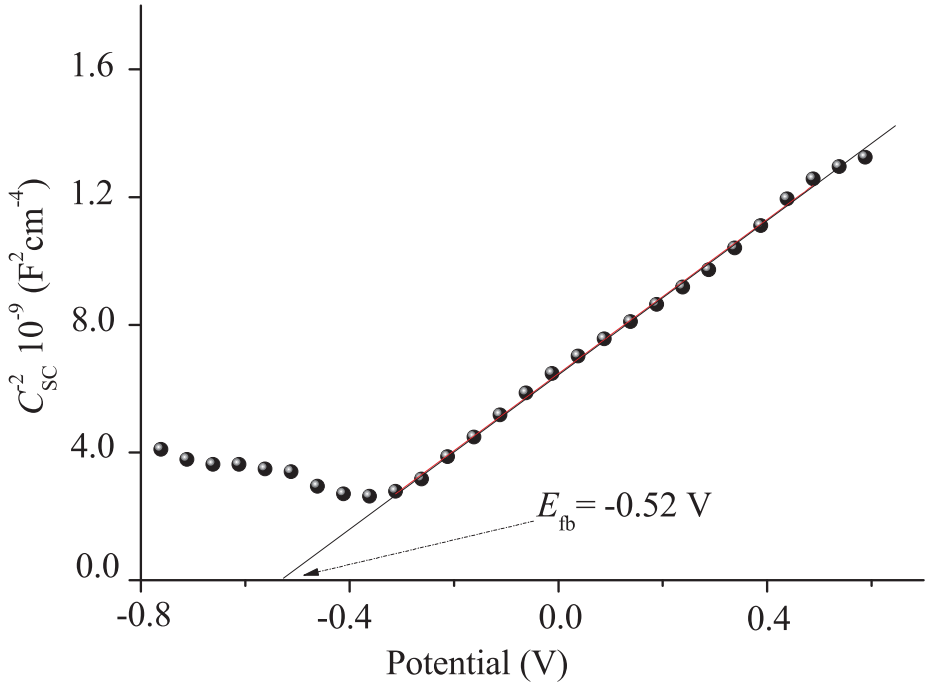

Fig. 9 The Mott–Schottky plot of *n*-type BBiTZS in neutral solution.

acteristic of high over voltages. The reduction peak at −0.5 V on the reverse scan indicates an irreversible process. Below ~−1.2 V, the current increases continuously with no plateau region, due to hydrogen liberation. The small exchange current J_o (0.2 μA cm^{-2}) and the polarization resistance (=10.7 kΩ cm^2) indicate a long-lived material (Fig. 8 Inset). For zero potential, the current density (J_o) is similar to an electron transfer rate constant.

The flat band potential (E_{fb}) is a key parameter in photo-electrochemistry, and it can be determined from the capacitance plot; its value (−0.56 V) is calculated by extrapolating the line (C_{SC}^{-2} − E) to infinite capacitance (C_{SC}^{-2} = 0). (Fig. 9). The energy diagram of the junction BBiTZS/solution, plotted from the photoelectrochemical characterization, predicts from a thermodynamic point of view the degradation of Rh B upon solar irradiation. The Rh B mineralization occurs by the reactive radicals OH· and $O_2^{\cdot-}$ respectively in the valence band (VB = 2.04 V) and conduction band (CB = -0.49 V); both the levels OH·/H_2O and $O_2/O_2^{\cdot-}$ are inside of the band gap (Roumila et al., 2016).

The EIS spectrum of the interface BBiTZS/Na_2SO_4 electrolyte was plotted once the free potential stabilized; it shows a semicircle at high frequencies ascribed to the charge transfer (SM 2). The impedance of the system is governed by the extension of the space charge region and the wide diameter is equal to the bulk resistance of the material R (27 kΩ cm^2) and the center positioned at −9° below the real axis, suggests an electron hopping by overcoming a low potential barrier. CP) is inserted to account for the non-ideality of the capacity (Aroutiounian et al., 2007; Aroutiounian et al., 2006):

$$Z = 1/(Q\ (j\omega)\ n) \tag{10}$$

As noted in the introduction, Rh B is a hazardous dye and its elimination is strongly motivated. The perovskite BBiTZS is promising in such a case owing to its attractive features i.e electronic bands appropriate localized and a gap E_g sensitive to the UV_A of the solar irradiance. The following sequences can be used to involve Rh-B mineralization via a photo-catalytic process:

$$BBiTZS + h\nu \rightarrow h^{+}_{VB} + e^{-}_{CB} \tag{11}$$

$$O_2 + e^{-}_{CB} \rightarrow O_2^{\cdot-} \tag{12}$$

$$2\ H_2O + O_2^{\cdot-} \rightarrow 4\ \cdot OH \tag{13}$$

$$H_2O + h^{+}_{VB} \rightarrow \cdot OH + H^{+} \tag{14}$$

$$O_2^{\cdot-} + H_2O + H^{+} \rightarrow \cdot OH + H_2O_2 + OH^{-} \tag{15}$$

$$H_2O_2 + e^{-}_{CB} \rightarrow OH^{-} + \cdot OH \tag{16}$$

$$OH^{-} + h^{+} \rightarrow \cdot OH \tag{17}$$

$$\cdot OH + \text{Rh B} \rightarrow \text{Products of oxidation} \tag{18}$$

Rh B is attacked by oxidative species ($O_2^{\cdot-}$, ·OH), resulting in a partial mineralization to CO_2 and H_2O (Bagtache et al., 2016). Fig. 10a illustrates the degradation mechanism on BBiTZS, which does not produce intermediate products, indicating that their concentrations are below the detection threshold of the spectrophotometer. Fig. 10b gives the photocatalytic evolution of Rh B conversion (10 mg L^{-1}) at various catalyst quantities. The decay in absorbance at 554 nm (λ_{max}) over the illumination time indicates a first order kinetic with a half-life of 90 min and a conversion yield of 50%.

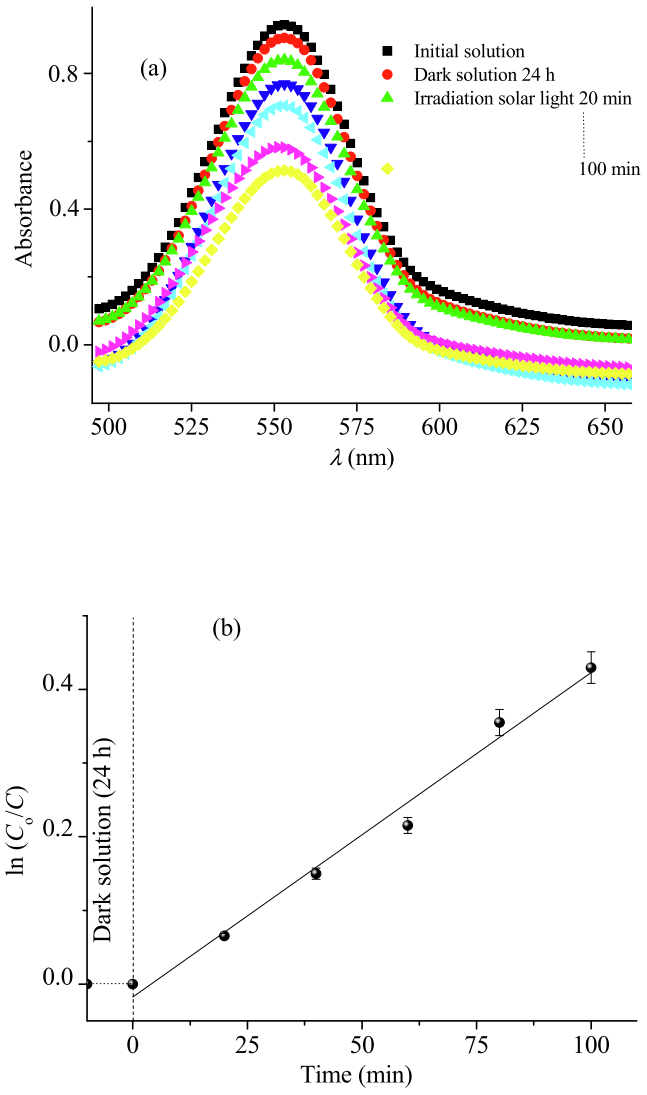

Fig. 10 (a) The UV–Visible spectra of RhB solutions on BBiTZS over illumination time. (b) The kinetic plot ln C_o/C vs. time. Experimental conditions: catalyst dose: 1 g/L; $[RhB]_o$ = 10 mg/L; V(solution) = 100 mL.

A comparison of the dye degradation with other relevant studies is reported in SM 3. One can conclude that the photoactivity of acceptable, compared with some previous studies, and BBiTZS could be used in photocatalysis.

4. Conclusion

In the summary, $Ba_{0.925}Bi_{0.05}(Ti_{0.65}Zr_{0.30}Sn_{0.05})O_3$ (BBiTZS) has been synthesized by solid state reaction and characterized by XRD, dielectric measurements and Raman spectroscopy. The Rietveld structural refinement at room temperature revealed a cubic perovskite structure. The dielectric properties showed a diffuse phase transition and ferroelectric relaxor behavior. This result was confirmed to the presence of a local structural disorder in the paraelectric phase due to the simultaneous incorporation of Bi^{3+} in the A-site and $(Zr\text{-}Sn)^{4+}$ in the B site, corroborated by the Raman spectroscopy. The energy diagram showed the potentiality of the lead-free ceramic BBiTZS for the photocatalytic applications because of the extended space charge region and environmentally friendly characteristic. The material showed a good Rh B photodegradation, and the conversion was followed by UV–Visible spectroscopy. On solar light, a conversion of 50% was determined in Rh B solution (10 mg L^{-1}) within 90 min., and the kinetic followed a first order model.

Declaration of Competing Interest

The authors declare that they have no known competing financial interests or personal relationships that could have appeared to influence the work reported in this paper.

Appendix A. Supplementary material

Supplementary data to this article can be found online at https://doi.org/10.1016/j.arabjc.2022.103744.

References

Ai, Z., Lu, G., Lee, S., 2014. Efficient photocatalytic removal of nitric oxide with hydrothermal synthesized $Na_{0.5}Bi_{0.5}TiO_3$ nanotubes. J. Alloy. Compd. 613, 260–266.

Alexe, M., Gruverman, A., Harnagea, C., Zakharov, N.D., Pignolet, A., Hesse, D., et al, 1999. Switching properties of self-assembled ferroelectric memory cells. Appl. Phys. Lett. 75 (8), 1158–1160.

Aroutiounian, V.M., Arakelyan, V.M., Shahnazaryan, G.E., Stepanyan, G.M., Khachaturyan, E.A., Wang, H., et al, 2006. Photoelectrochemistry of semiconductor electrodes made of solid solutions in the system Fe_2O_3–Nb_2O_5 Available from: Sol. Energy 80 (9), 1098–1111 https://www.sciencedirect.com/science/article/pii/S0038092X05003609.

Aroutiounian, V.M., Wang, H., Turner, J.A., 2007. Photoelectrochemistry of tin-doped iron oxide electrodes. Sol. Energy 81, 1369–1376.

Bagtache, R., Abdmeziem, K., Rekhila, G., Trari, M., 2016. Synthesis and semiconducting properties of Na_2MnPO_4F. Application to degradation of Rhodamine B under UV-light. Mater. Sci. Semicond. Process. 51, 1–7. https://doi.org/10.1016/j.mssp.2016.04.016.

Bensemma, N., Rekhila, G., Boutal, N., Taıbi, K., Trari, M., 2018. Photoelectrochemical properties of lead-free ferroelectric ceramic $Ba(Ti_{0.96}Mg_{0.013}Nb_{0.026})O_3$: application to solar conversion of eosin. J. Mater. Sci: Mater. Electron. https://doi.org/10.1007/s10854-016-4625-z.

Benyoussef, M., Zannen, M., Belhadi, J., Manoun, B., Dellis, J.L., Lahmar, A., el Marssi, M., 2020. Complex impedance and Raman spectroscopy of Na0.5(Bi1-xDyx)0.5TiO3 ceramics. Ceram. Int. 46, 10979–10991. https://doi.org/10.1016/J.CERAMINT.2020.01.114.

Boultif, A., Loueer, D., 1991. Indexing of powder diffraction patterns for low-symmetry lattices by the successive dichotomy method. J. Appl. Crystallogr. 24 (pt 6), 987–993.

Boutal, N., Rekhila, G., Taïbi, K., Trari, M., 2014. Relaxor ferroelectric and photo-electrochemical properties of lead-free $Ba_{1-x}Eu_{2x/3}(Ti_{0.75}Zr_{0.25})O_3$ceramics. Application to chromate reduction. Sol. Energy 99, 291–298.

Burbure, N.V., Salvador, P.A., Rohrer, G.S., 2010a. Photochemical reactivity of titania films on $BaTiO_3$ substrates: Influence of titania phase and orientation. Chem. Mater. 22 (21), 5831–5837.

Burbure, N.V., Salvador, P.A., Rohrer, G.S., 2010b. Photochemical reactivity of titania films on $BaTiO_3$ substrates: Origin of spatial selectivity. Chem. Mater. 22 (21), 5823–5830.

Ciomaga, C., Viviani, M., Buscaglia, M.T., Buscaglia, V., Mitoseriu, L., Stancu, A., 2007. Preparation and characterization of the Ba(Zr, Ti)O_3 ceramics with relaxor properties. J. Eur. Ceram. Soc. 27, 4061–4064. https://doi.org/10.1016/j.jeurceramsoc.2007.02.095.

Cross, L.E., 1994. Relaxor ferroelectrics: an overview. Ferroelectrics 151, 305–320. https://doi.org/10.1080/00150199408244755.

Cui, Y., Briscoe, J., Dunn, S., 2013. Effect of Ferroelectricity on Solar-Light-Driven Photocatalytic Activity of BaTiO3: Influence on the Carrier Separation and Stern Layer Formation. Chem. Mater. 25, 4215–4223.

Directive 2011/65/EU of the European Parliament and of the Council of 8 June 2011 on the Restriction of the Use of Certain Hazardous Substances in Electrical and Electronic Equipment Text with EEA Relevance, 2011. http://data.europa.eu/eli/dir/2011/65/oj/eng.

Dobal, P.S., Dixit, A., Katiyar, R.S., Yu, Z., Guo, R., Bhalla, A.S., 2001. Micro-Raman scattering and dielectric investigations of phase transition behavior in the $BaTiO_3$–$BaZrO_3$ system. J. Appl. Phys. 89, 8085–8091. https://doi.org/10.1063/1.1369399.

Giocondi, J.L., Rohrer, G.S., 2001. Spatial Separation of Photochemical Oxidation and Reduction Reactions on the Surface of Ferroelectric $BaTiO_3$. J. Phys. Chem. B. 105 (35), 8275–8277.

Haddadou, N., Bensemma, N., Rekhila, G., Trari, M., Taïbi, K., 2018a. Photoelectrochemical properties of the relaxor $Ba(Ti_{0.90}Sc_{0.05}Nb_{0.05})O_3$: application to the degradation of amoxicillin under solar light. J. Mater. Sci.: Mater. Electron. Springer, US 29 (6), 5042–5048. https://doi.org/10.1007/s10854-017-8466-1.

Haddadou, N., Belhadi, J., Manoun, B., Taïbi, K., Carcan, B., El Marssi, M., Lahmar, A., 2018b. Structural, vibrational and dielectric investigations of $Ba_{0.925}Bi_{0.05}(Ti_{0.95-x}Zr_x)Sn_{0.05}O_3$ ceramics. J. Mater. Sci.: Mater. Electron. https://doi.org/10.1007/s10854-018-9703-y.

Jiwei, Z., Xi, Y., Liangying, Z., Bo, S., Chen, H., 2005. Thin Films Grown by a Sol-Gel Process. Ferroelectrics 329, 23–27.

Kappadan, Shabina, Gebreab, Tesfakiros Woldu, Thomas, Sabu, Kalarikkal, Nandakumar, 2016. Tetragonal $BaTiO_3$ nanoparticles: An efficient photocatalyst for the degradation of organic pollutants. Mater. Sci. Semicond. Process. 51, 42–47.

Kenji uchino, 1994. Relaxor ferroelectric devices. Ferroelectrics 151 (1), 321–330.

Kerfah, A., Taïbi, K., Omeiri, S., Trari, M., 2011. Relaxor ferroelectric and photocatalytic behaviour of $Ba_{0.785}Bi_{0.127}Y_{0.017}TiO_3$composition. Sol. Energy 85 (3), 443–449.

Lanfredi, S., Carvalho, J.F., Hernandes, A.C., 2000. Electric and dielectric properties of Bi12TiO20 single crystals. J. Appl. Phys. 88, 283. https://doi.org/10.1063/1.373654.

Laulhé, C., 2007. Zr B. Structure locale dans un ferroélectrique relaxeur : $BaTi_{1-x}$ Zr $_xO_3$ To cite this version : HAL Id : tel-00196922.

Li, Z., Wang, Y., Liu, J., Chen, G., Li, Y., Zhou, C., 2009. Photocatalytic hydrogen production from aqueous methanol solutions under visible light over $Na(Bi_xTa_{1-x})O_3$. Int. J. Hydrogen Energy 34, 147–152.

Lin, X., Xing, J., Wang, W., Shan, Z., Xu, F., Huang, F., 2007. Photocatalytic activities of heterojunction semiconductors Bi_2O_3/$BaTiO_3$: A strategy for the design of efficient combined photocatalysts. J. Phys. Chem. C 111 (49), 18288–18293.

Nag Bhargavi, G., Khare, A., Badapanda, T., Ray, P.K., Brahme, N., 2018. Influence of Eu doping on the structural, electrical and optical behavior of Barium Zirconium Titanate ceramic. Ceram. Int. 44, 1817–1825. https://doi.org/10.1016/j.ceramint.2017.10.116.

Park, B.H., Kang, B.S., Bu, S.D., Noh, T.W., Lee, J., Jo, W., 1999. Lanthanum substituted bismuth titanate for use in non-volatile memories. Nature 40, 682.

Qi, W., Wang, Y., Jiyue, W., Zimeng, H., Jia, C., Zhang, H., 2019. Relaxor ferroelectric and photocatalytic properties of BaBi4-Ti4O15. Adv. Appl. Ceram., 1–7 https://doi.org/10.1080/17436753.2019.1634943.

Reddy, N.L., Reddy, G.K., Basha, K.M., Mounika, P.K., Shankar, M.V., 2016. ScienceDirect highly efficient hydrogen production using Bi_2O_3/TiO_2 nanostructured photocatalysts under led light irradiation. Materials Today: Proc. 3 (6), 1351–1358.

Rekhila, G., Gabes, Y., Bessekhouad, Y., Trari, M., 2018. Hydrogen production under visible illumination on the spinel $NiMn_2O_4$ prepared by sol gel. Solar Energy 166, 220–225. https://doi.org/10.1016/j.solener.2018.02.064.

Rodríguez-Carvajal, J., 2002. An Introduction ToThe PROGRAM (2001), 1–139.

Roumila, Y., Abdmeziem, K., Rekhila, G., Trari, M., 2016. Semiconducting properties of hydrothermally synthesized libethenite application to orange G photodegradation. Mater. Sci. Semicond. Process. 41, 470–479. https://doi.org/10.1016/j.mssp.2015.10.018.

Schileo, G., Luisman, L., Feteira, A., Deluca, M., Reichmann, K., 2013. Structure – property relationships in $BaTiO_3$–$BiFeO_3$–$BiYbO_3$. Ceramics 33, 1457–1468.

Smail, S. et al, 2020. Structural, dielectric, electrocaloric and energy storage properties of lead free $Ba_{0.975}La_{0.017}(Zr_xTi_{0.95-x})Sn_{0.05}O_3$ (x = 0.05; 0.20) ceramics. Mater. Chem. Phys. 252, 123462.

Tang, X.G., Wang, J., Wang, X.X., Chan, H.L.W., 2004. Effects of grain size on the dielectric properties and tunabilities of sol-gel derived $Ba(Zr_{0.2}Ti_{0.8})O_3$ ceramics. Solid State Commun. 131 (3–4), 163–168.

Tang, X.G., Wang, X.X., Chew, K.H., Chan, H.L.W., 2005. Relaxor behavior of (Ba, Sr)(Zr, Ti)O_3 ferroelectric ceramics. Solid State Commun. 136 (2), 89–93.

Uchino, K., Nomura, S., 1982. Critical exponents of the dielectric constant in diffusedphase-transition crystals. Ferroelectr. Lett. 44, 55e61.

Uchino, K., Sadanaga, E., Hirose, T.J., 1989. J. Am. Ceram. Soc. 72, 1555–1558.

Viehland, D., Wuttig, M., Cross, L.E., 1991. The glassy behavior of relaxor ferroelectrics. Ferroelectrics 120, 71–77.

Wang, Tong, Hu, Jiacong, Yang, Haibo, Jin, Li, Wei, Xiaoyong, Li, Chunchun, Yan, Fei, Lin, Ying, 2017. Dielectric relaxation and Maxwell-Wagner interface polarization in Nb2O5 doped 0.65BiFeO3–0.35BaTiO3 ceramics. J. Appl. Phys. 121, 084103. https://doi.org/10.1063/1.4977107.

Wang, Tong, Liu, Jiaqi, Kong, Luo, Yang, Haibo, Li, Chunchun, 2020. Evolution of the structure, dielectric and ferroelectric properties of $Na_{0.5}Bi_{0.5}TiO_3$-added $BaTiO_3$–$Bi(Mg_{2/3}Nb_{1/3})O_3$ ceramics. Ceramics International 46, 25392–25398. https://doi.org/10.1016/j.cap.2013.09.016.

Wang, L., Wang, W., 2012. Photocatalytic hydrogen production from aqueous solutions over novel $Bi_{0.5}Na_{0.5}TiO_3$ microspheres. Int. J. Hydrogen Energy 37 (4), 3041–3047.

Wang, Yuanhao, Wang, Tong, Wang, Jiahui, Liu, Jiaqi, Xing, Zhuo, Yang, Haibo, Kong, Luo, Cheng, Yan, Chen, Guanjun, Wang, Fen, Li, Chunchun, 2021. A-site compositional modulation in barium titanate based relaxor ceramics to achieve simultaneously high energy density and efficiency. J. Eur. Ceramic Soc. 41, 6474–6481.

Xiaoyong, W., Yujun, F., Xi, Y., 2003. Dielectric relaxation behavior in barium stannate titanate ferroelectric ceramics with diffused phase transition. Appl. Phys. Lett. 83 (10), 2031–2033.

Yang, W.-C., Rodriguez, B.J., Gruverman, A., Nemanich, R.J., 2005. Photo electron emission microscopy of polarity-patterned materials. J. Phys.: Condens. Matter 17 S1415.

Yang, Y., Sun, Y., Jiang, Y., 2006. Structure and photocatalytic property of perovskite and perovskite-related compounds. Mater. Chem. Phys. 96 (2–3), 234–239.